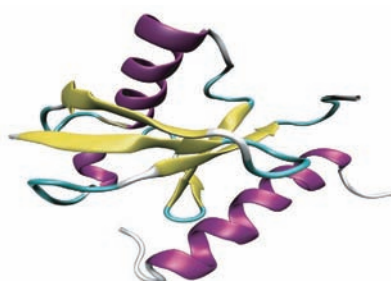


TSUBAME ESJ.



Ab initio NMR Chemical Shift Calculations
for Biomolecular Systems
Using Fragment Molecular Orbital Method

A Large-scale Two-phase Flow Simulation
on GPU Supercomputer

Evolutionary Image/
Video Coding with Massively Parallel Computing



Ab initio NMR Chemical Shift Calculations for Biomolecular Systems Using Fragment Molecular Orbital Method

Qi Gao*/** Satoshi Yokojima** Shinichiro Nakamura** Minoru Sakurai*

* Center for Biological Resources and Informatics, Tokyo Institute of Technology

**Mitsubishi Chemical Group Science and Technology Research Center, Inc.

We have developed two types of fragment molecular orbital (FMO)-based NMR chemical shift calculation methods. They successfully lead to a dramatic reduction of the computational costs by dividing one molecular system into small subsystems and then carrying out calculations on the subsystems in a parallel fashion. Several case studies show that the chemical shift values calculated by our FMO-based methods are in good agreement with those obtained by the standard methods for chemical shift calculation. Our works demonstrate that parallel quantum chemical calculations using a powerful computational resource such as TSUBAME enable us to study a wide range of physical properties of large biomolecules with high accuracy in short time.

Introduction

1

In NMR spectroscopy, the chemical shift describes the dependence of nuclear magnetic energy levels on the electronic environment in a molecule. In other words, it is a parameter that corresponds to the difference in resonance frequency between nuclei placed in different molecular environments. This means that the chemical shift is sensitive to various physicochemical factors such as molecular conformation, configuration, chemical composition, and surrounding solvent. Thus, observation of chemical shift, usually combined with those of other NMR parameters (i.e. J-coupling, relaxation time and NOE), can provide invaluable information on the three-dimensional structures of molecules, especially in solution.

However, for large molecules like proteins, it is difficult to correctly assign their chemical shifts to corresponding 3D structures only by using experimental approaches. For accurate structural analysis based on the chemical shift observation, it is necessary to obtain the information on how the electronic wave function of a molecule is perturbed by its conformational and other structural changes. Therefore, theoretical approaches play an essential role in determining and refining molecular structures in the framework of NMR spectroscopy. Our work is concerned with the development of chemical shift calculations for protein on the basis of quantum mechanics.

Chemical shift in large molecular systems has long been considered too complicated, or even impossible to be studied by conventional quantum chemistry calculations. The major problem concerns the computational cost of calculating chemical shift. For reliable estimates of chemical shifts, high-level quantum chemical calculations, based on coupled perturbed methods, are required. Unfortunately, these methods are computationally very inefficient and can be applied to small isolated molecules only.

In this work, we combine well-established *ab initio* methods for chemical shift calculation with the FMO method, which allows for a rapid calculation for a large molecule by dividing it into small fragments. In particular, we have used this combined method to predict the total chemical shifts of ubiquitin, a small (76 residues) and highly-conserved regulatory protein [1]. Furthermore, to improve the accuracy of this FMO based NMR chemical shift calculation method, we develop a method capable of defining an appropriate fragment size, i.e. a cutoff distance, to better reproduce the chemical shift values^[2,3].

NMR calculations

2

Chemical shift can be evaluated theoretically by solving the Schrödinger equation in which hamiltonian includes a vector potential corresponding to the external magnetic field. Here, we face a new problem. Because we inevitably use finite basis sets, the calculated chemical shifts depend on the location of gauge origin of the vector potential. In order to find a numerical solution for the nuclear magnetic shielding tensor without the gauge origin dependence, in practice two methods are proposed and established; the GIAO^[4] and CSGT^[5].

The GIAO method calculates nuclear magnetic shielding tensor $\sigma_{\alpha\beta}$ as mixed derivatives of the energy E with respect to an external magnetic field \mathbf{B} and nuclear magnetic moment μ . The gauge origin dependence is eliminated by using field-dependent atomic orbitals.

$$\sigma_{\alpha\beta} = \frac{\partial^2 E}{\partial \mu_\alpha \partial B_\beta} \quad (1)$$

The CSGT method calculates the tensor $\sigma_{\alpha\beta}$ as the linear response to an external uniform magnetic field \mathbf{B} at the nuclear

Ab initio NMR Chemical Shift Calculations for Biomolecular Systems Using Fragment Molecular Orbital Method

position \mathbf{r}_N , where $\mathbf{J}^{(1)}(\mathbf{r})$ is the induced first-order electronic current density.

$$\sigma_{\alpha\beta}(\mathbf{r}_N) = -\frac{\mu_0}{4\pi} \int d^3\mathbf{r} \left[\frac{\partial \mathbf{J}^{(1)}(\mathbf{r})}{\partial B_\beta} \times \frac{\mathbf{r}_N - \mathbf{r}}{|\mathbf{r}_N - \mathbf{r}|^3} \right]_\alpha \quad (2)$$

In the CSGT method, the gauge problem is addressed by redefining the gauge origin \mathbf{R}_0 as a parametric function that depends on the position at which induced current is evaluated.

The chemical shift, δ , is related to the nuclear magnetic-shielding tensor, $\sigma_{\alpha\beta}$, by a reference standard, σ^0 , as

$$\delta = (\sigma^0 - \sigma^{\text{iso}}) / (1 - \sigma^0) \times 10^6 \approx (\sigma^0 - \sigma^{\text{iso}}) \times 10^6$$

with the absolute isotropic shielding constant,

$$\sigma^{\text{iso}} = \text{Tr}(\sigma_{\alpha\beta}) / 3$$

FMO method

3

At the restricted Hartree-Fock (RHF) level of conventional quantum chemistry theory, the energy E of a molecule is calculated by solving the following equation

$$\tilde{\mathbf{F}}\mathbf{C} = \mathbf{S}\mathbf{C}\boldsymbol{\varepsilon} \quad (3)$$

where \mathbf{F} is the Fock matrix, \mathbf{C} is a matrix of molecular orbital coefficients and \mathbf{S} is the overlap matrix.

The computational time required to solve the equations of the Hartree-Fock (HF) theory increases rapidly $O(N^{3-4})$ with system size N ; as a result, application of conventional *ab initio* methods to biomolecules is too expensive. Therefore, the size of a typical condensed phase system, such as fully solvated proteins, necessitates the use of fragment molecular orbital (FMO) method.

In the FMO method, a large molecule is divided into N small fragments (monomers). Then the total energy is given by

$$E = \sum_I E_I + \sum_{I>J} (E_{IJ} - E_I - E_J) \quad (4)$$

where the sum are over monomer E_I and dimer E_{IJ} (pairs of any two monomers) in the molecule. In the RHF level the contributions to the total energy due to monomer and dimer can be calculated by

$$\tilde{\mathbf{F}}^x \mathbf{C}^x = \mathbf{S}^x \mathbf{C}^x \boldsymbol{\varepsilon}^x \quad (5)$$

where superscript x represents monomers ($x=I$) and dimers ($x=IJ$). Here, the RHF calculations of all the monomers and dimers are performed in the electrostatic potential (ESP) created by the whole system. The ESP is determined by repeatedly solving the RHF equation of each monomer until the energy converges self-consistently. Finally, the RHF equation of every dimer is solved once including the ESP determined by the previous monomer FMO calculations. The diagram showing the various steps in the FMO method is given in Figure 1. Previous FMO studies^[6-8] of biomolecular systems showed that FMO dimer calculation has a good compromise between the attained accuracy and the computational cost incurred.

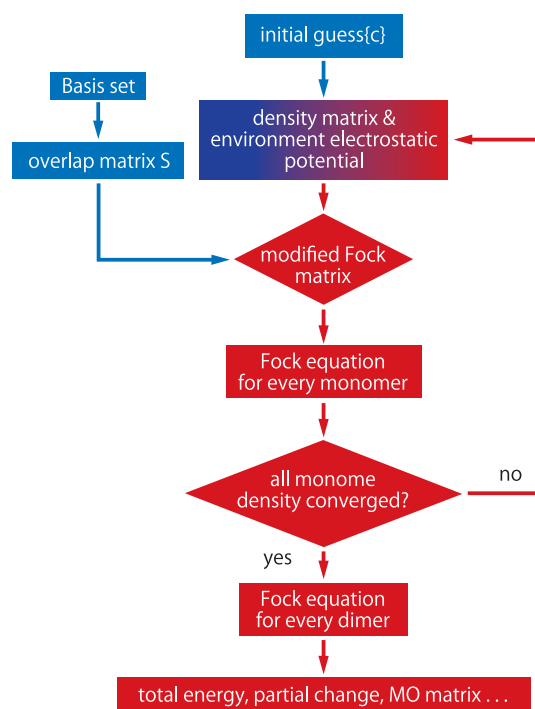


Figure 1 Computational flow scheme of a typical FMO2 scheme. Every monomer enter the self-consistent field routine, with the electrostatic potential added to the Hamiltonian used to create the Fock matrix \mathbf{F} . the calculation keeps running until every monomer converges at the same time.

FMO-NMR calculation

4

By combining the FMO method with either GIAO or CSGT methods, we have developed two computational models for calculating chemical shift of large biomolecular systems. Model-I is a method, in which the shielding tensors of one fragment are calculated in a point charge environment (*i.e.* the ESP from other fragments is replaced by point charges on other fragments). The point charge environment can be constructed through the density matrix of every monomer. Model-II uses the ESP of other fragments without any approximation. We first calculate Fock matrix dimers which are built upon neighboring monomer pairs, by solving

$$\tilde{\mathbf{F}}^{IJ} = \tilde{\mathbf{H}}^{IJ} + \mathbf{G}^{IJ} \quad (J-I=1) \quad (6)$$

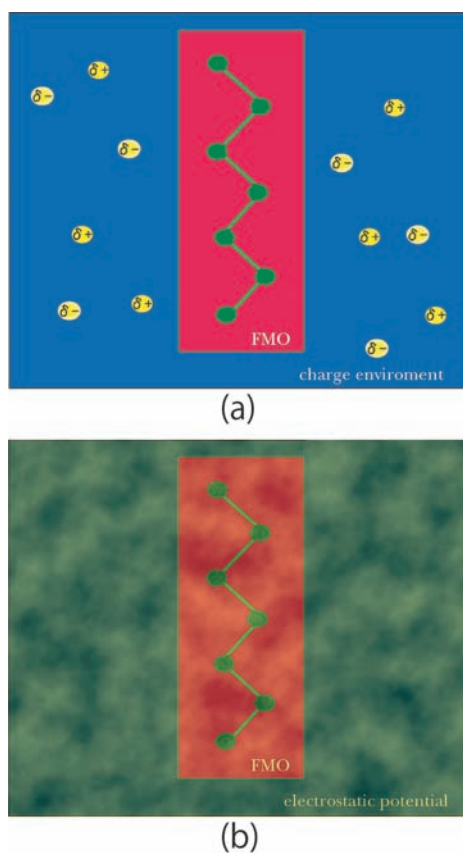


Figure 2 Illustration of the FMO-NMR calculation concept. Chemical shifts of target fragment (red block region) are calculated by using surrounding point charge (Model-I (a)) or charge density distribution (Model-II (b)) to represent the effects of surrounding chemical

and then perform CPHF calculation directly using the Fock matrix to obtain the shielding tensor of the atoms in dimer. The GIAO method is adopted into Model-I, whereas the CSGT method is adopted into both Model-I and Model-II^[1]. These two models are illustrated in Figure 2.

We selected the ubiquitin protein as a representative example of a large biological molecule. The results for the ¹³C, ¹⁵N and ¹H chemical shifts, which are calculated by our method at the 6-31G(d) level, are shown in Figures 3, and are compared with the experimentally observed values.

The chemical shifts of all the atom types are in fairly good agreement with the experimental data. For example, the mean errors of ¹³C_α are 1.20 ppm and 1.59 ppm for Model I/GIAO and Model I/CSGT, and 1.68 ppm for Model II/CSGT. The standard deviation is 1.16 ppm and 1.65 ppm for Model I/GIAO and Model I/CSGT and 1.64 ppm for Model II/CSGT. However, the max errors are still larger than the required accuracy especially for ¹⁵N and ¹H atoms, which are much more sensitive to the local environment effects than those of the ¹³C atoms. Thus, these results stress the need of effectively taking into account local environment effects for an accurate representation of electron cloud around atoms in order to achieve our desired accuracy.

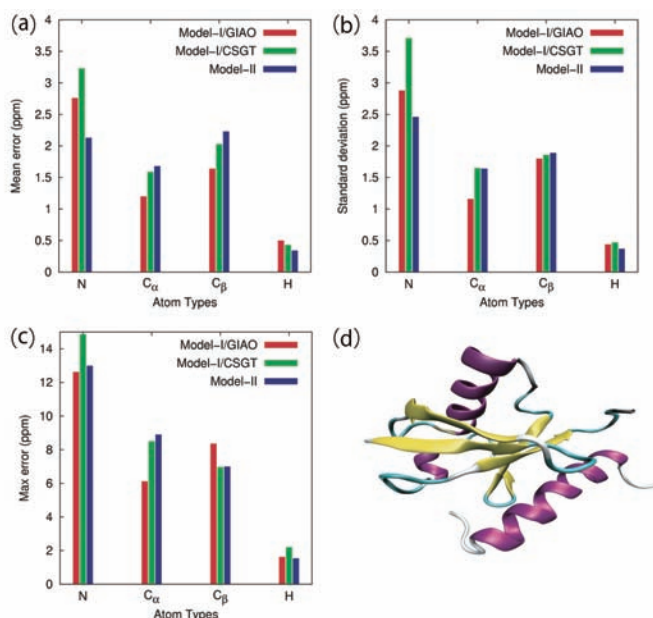


Figure 3 Quality of chemical shifts (a-c) (relative to experiment) of ubiquitin (d) atoms calculated with FMO-NMR method (6-31G(d)).

FMO(merged)-NMR calculation

5

Although the FMO-NMR method could reproduce well the corresponding experimental and conventional *ab initio* calculated chemical shift data^[1], errors of all the atom types were still larger than the desired level, which is in the range of 1 ppm for heavy atoms and 0.3 ppm for hydrogen atoms. To obtain an improved accuracy of calculation results, we proposed a modification to the FMO-NMR method by introducing the concept of a merged fragment with a cutoff distance, which defines the optimal merged fragment size for NMR calculations. We called the method as FMO(merged)-NMR method.

In the FMO(merged)-NMR method, the point charge (Model-I) and charge density (Model-II) of every fragment are first obtained from FMO monomer calculations. Then, a merged fragment is constructed by assembling all the fragments within a cutoff distance from the center of target monomer. Subsequently, the Fock matrix of this merged fragment is evaluated with taking into account the effect of the surrounding chemical environment. Finally, the Fock matrix is used to perform the GIAO and CSGT methods to obtain chemical shift values of the target monomer. Illustrations of the FMO(merged)-NMR method in Model-I and Model-II are given in Figure 4.

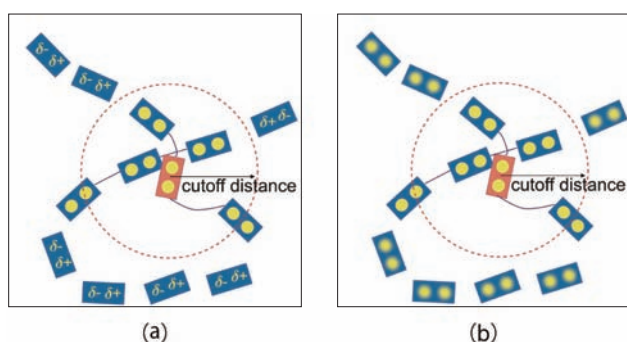


Figure 4 Schematic representation of the FMO (merged)-NMR method. A cutoff distance is used to determine the optimal fragment size (i.e. merged fragment) for accurately calculating the chemical shift of target monomer (orange block region) in both Model-I (a) Model-II (b).

A β -sheet peptide, which is from residues 198 to 229 in green fluorescent protein (GFP), was selected to evaluate the performance of the FMO(merged)-NMR method. Here, the cutoff distance was set to 10 Å value which is large enough to accurately reproduce the surrounding effects^[9].

In Figure 5, the errors of chemical shifts are given as deviations from the calculated values obtained by the conventional *ab initio* methods. For all the atom types studied, the errors of the FMO(merged)-NMR calculations are much smaller than those of the FMO-NMR calculation. For example, in the case of the chemical shifts of carbon atoms ($^{13}\text{C}_\alpha$ and $^{13}\text{C}_\beta$), the FMO-NMR calculations give isotropic shielding constants with a larger maximum error of less than 3.88 ppm and a mean error of less than 0.89 ppm in Model-II^[2], whereas the FMO1(merged)-NMR calculations reduces both the maximum and absolute mean errors of chemical shifts of carbon atoms, i.e., to less than 0.15 and 0.05 ppm, respectively. These results indicate that the FMO(merged)-NMR method provides a much more accurate local chemical environment description around the atom of interest than does the FMO-NMR method.

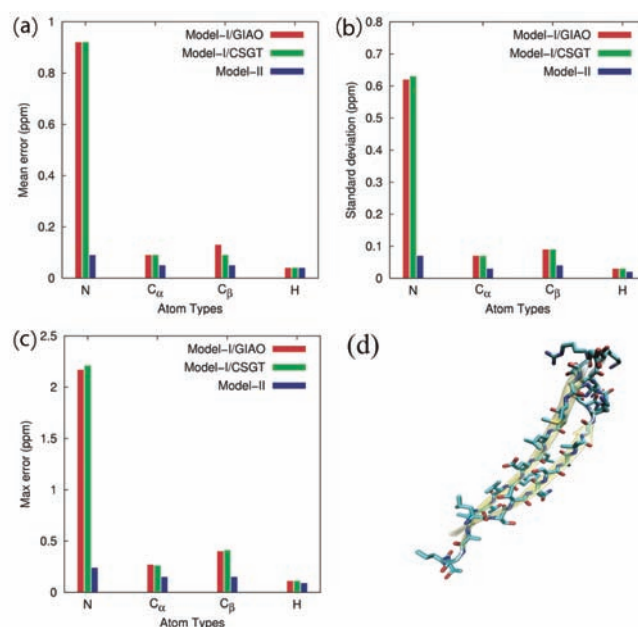


Figure 5 Quality of chemical shifts (a-c) relative to conventional *ab initio* calculation results of a β -sheet (d) atoms in green fluorescent protein calculated with FMO(merged)-NMR method (6-31G(d)).

Summary

6

The aim of the work presented here is to develop an *ab initio* method for accurately predicting chemical shifts of large biomolecular systems in short time. Although accuracy and speed are usually incompatible in quantum chemical calculations, we solved this by introducing the FMO method to obtain the wave function of a molecule. In our early developed method, called the FMO-NMR method, basically the dimer fragment is used to calculate the chemical shifts of target amino acid. This method reproduced well the experimental chemical shifts of ubiquitin, but with the max errors larger than our required accuracy especially for ^{15}N and ^1H atoms, which are much more sensitive to the local environment effects. To address this issue, we developed a modified method, called FMO(merged)-NMR method, in which a cutoff distance was introduced to define an optimal fragment for accurately reproducing the local environmental effects. We applied this modified method to one of the β -sheet peptides in GFP and the resultant chemical shift values were in excellent agreement with those calculated by the conventional *ab initio* NMR calculations. Thus, the FMO(merged)-NMR method is recommended for future chemical shift calculations in large biomolecular systems.

Quantum chemical calculations can help us to look at a nano-scale part of the physical universe which contains many unknown phenomena and mechanisms. However, the computational demand of conventional quantum chemistry methods is so large that they can be applied only to small isolated molecules. Our work demonstrated that the formulation of theory appropriate for parallel computation and the use of a powerful computational resource such as TSUBAME enable us to conquer such a drawback. Our work has opened up the possibility to use similar approaches to study a wide range of physical properties of large biomolecules.

References

- [1] Gao, Q.; Yokojima, S.; Kohno, T.; Ishida, T.; Fedorov, D. G.; Kitaura, K.; Fujihira, M.; Nakamura, S. Chem. Phys. Lett. 2007, 445, 331.
- [2] Yokojima, S.; Gao, Q.; Nakamura, S. AIP Conf. Proc. 2009, 1102, 164.
- [3] Gao, Q.; Yokojima, S.; Fedorov, D. G.; Kitaura, K.; Sakurai, M.; Nakamura, S. J. Chem. Theory Comput. 2010, 6, 1428.
- [4] Ditchfield, R. Mol. Phys. 1974, 27, 789.
- [5] Keith, T. A.; Bawder, R. F. W. Chem. Phys. Lett. 1993, 210, 223.
- [6] Fedorov, D. G.; Kitaura, K.; in: Starikov, E. B.; Lewis, J. P.; Tanaka, S. (Eds.), Modern Methods for Theoretical Physical Chemistry of Biopolymers, Elsevier, Amsterdam, 2006.
- [7] Fedorov, D. G.; Kitaura, K. J. Chem. Phys. 2004, 120, 6832.
- [8] Fedorov, D. G.; Kitaura, K. J. Chem. Phys. 2004, 389, 129.
- [9] Sitkoff, D.; Case, D. A. Prog. NMR Spectr. 1998, 32, 165.

A Large-scale Two-phase Flow Simulation on GPU Supercomputer

Takayuki Aoki* Kenta Sugihara**

* Global Scientific Information and Computing Center, Tokyo Institute of Technology

**Graduate School of Engineering, Tokyo Institute of Technology

Two-phase flows such as gas-water mixing are often observed in nature; however, their numerical simulation is one of the most challenging themes in computational fluid dynamics, and it takes a long computational time.

A state-of-the-art interface capture method, sparse matrix solver, higher-order advection scheme, and others have been introduced and entirely implemented for GPU computing. It has become possible to carry out large-scale two-phase flow simulations that have never been achieved before. In a violent air-water flow, small bubbles entrained in the water are described clearly and good performance scalability is also shown for multi-GPU computing.

Introduction and Motivation

1

Recently movie scenes of violent flows mixing air with water have been produced by computer graphics in Hollywood film productions. It is notable that they carry out larger-scale computations with higher-resolution than those of scientific and engineering works. For two-phase flows, particle methods such as SPH (smoothed particle hydrodynamics) have been used due to the simple algorithm and success of astrophysical N-body simulation in the beginning of GPU computing. Each particle interacts with all particles within the kernel radius to compute the particle motion. In three-dimensional simulation, the number of interacting particles increases, and particle methods have disadvantages from the viewpoints of numerical accuracy, random memory access, and amount of computation. In particular, the sparse matrix for the pressure Poisson equation has a wide bandwidth of non-zero elements in the semi-implicit time integration and is inefficiently solved in such memory distributed systems as multi-node clusters or supercomputers. In addition, there are problems involving non-physical oscillation at the gas-liquid interface, inaccurate evaluation of the surface tension, and large numerical viscosity.

In mesh methods such as FDM (finite difference method), FVM (finite volume method), and FEM (finite element method), the computation for a mesh point, a cell, or an element requires only accesses to some neighboring points. Higher-order numerical schemes are easily applicable to the FDM in structured meshes. In Hollywood film productions, they have changed the particle methods to mesh methods to make realistic water scenes. In a mesh method, the gas and liquid phases are treated as one fluid with different material properties: density, viscosity, and surface tension. It is necessary to introduce an

interface capturing technique to identify the different properties. The density changes 1000 times from the gas to the liquid at the interface, and the profile is expressed with a few meshes.

In this article, we show a large-scale gas-liquid two-phase simulation by full GPU computing, which has never been achieved before.

Gas-liquid interface capturing method

2

The gas-liquid interface is often described as a surface of a three-dimensional identical function. The 3-D information seems to be too much for the 2-D surface information; however, the method makes it easy to express such topology changes as splitting and merging of bubbles. The Level-Set function^[1] and the VOF (volume of fluid) are often used as an identical function. The former is a signed distance function from the interface as shown in Fig.1. In the gas region, it has negative distance, and in the liquid region, it has positive distance. The interface is expressed as the zero-level iso-surface of the smooth profile, which is able to accurately trace the interface.

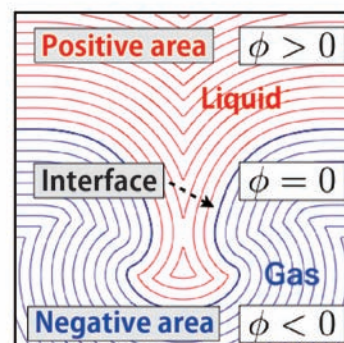


Figure 1 Iso-surface plots of the Level-Set function

**Current position: Japan Atomic Energy Agency

The Level-Set method cannot guarantee conservation of the volumes of the gas and the liquid. We lose small bubbles and droplets during the computation. On the other hand, the VOF method conserves the volume and has poor interface shapes when the curvature radius comes closer to the mesh size.

We introduce the VOF-based THINC^[3] WLIC^[4] method to our simulation, in which the anti-diffusion keeps the interface sharp. We apply the Level-Set method only to evaluate the interface curvature and the contact angle.

Incompressible Navier-Stokes Solver

3

3-1 Advection term

For the advection terms of the Navier-Stokes equation and re-initializing the Hamilton-Jacobi equation, we used the 5th-order WENO scheme. The high-wavelength filter to preserve monotonicity contributed the numerical stability. Figure 2 illustrates the stencil access of the 5th WENO scheme. When the on-chip shared memory was used as a software-managed cache, we reduced the same access to the off-chip memory (recently the L1 cache is available for this purpose in Fermi-core GPU). For this part, we have achieved more than 300 GFLOPS on the NVIDIA GTX 280.

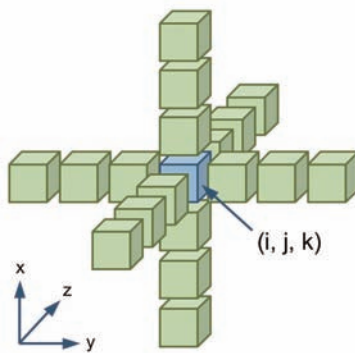


Figure 2 Stencil of the 5th WENO scheme.

3-2 Pressure Poisson Solver

It takes a major portion of the computational time to solve the pressure Poisson equation for two-phase flows. In the case of a structured mesh, non-zero elements are located regularly in the sparse matrix; however, their values change 1000 times. We have developed the BiCGStab method in the Krylov sub-space iteration in collaboration with MIZUHO Information and Research Institute as a GPU matrix library. The convergence was drastically improved

by coupling with a V-cycle multi-grid preconditioner shown in Fig. 3. In the multi-grid process, the ILU method was applied to the smoother with the Red and Black algorithm.

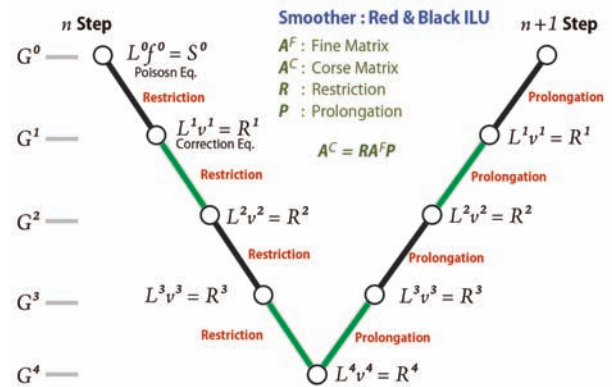


Figure 3 V-cycle of the multi-grid preconditioner.

Single Bubble Rising

4

To confirm the gas-liquid two-phase flow simulation, we compared it with the experiment of a single bubble rising. In accordance with the Grace diagram^[5], the bubble shape can be spherical, ellipsoidal, skirted, or dimpled, depending on the dimensionless parameters: Eotvos number (Eo), Morton number (Mo), and Reynolds number (Re). For such parameters, the simulation results are in good agreement with the experimental shapes and rising speeds^[6].

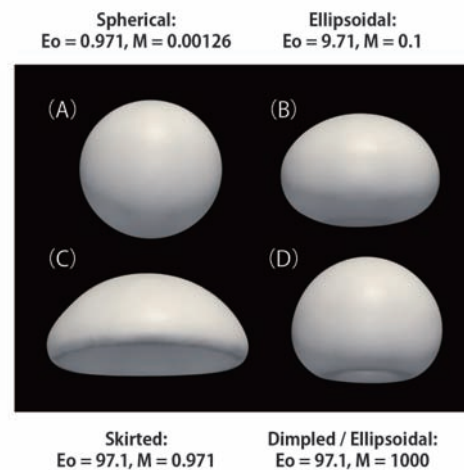


Figure 4 Bubble shapes depending on Eotvos number (Eo) and Morton number (Mo).

Milk-crown Formation

5

It is well known that a milk crown is formed by dropping a droplet into a glass of shallow milk, and its mechanism and the number of fingers is still being discussed. The simulation for a liquid with the same viscosity, surface tension, and impact velocity as the experiment by Krechetnikov ^[7] was carried out. Figure 5 exhibits the typical shape of the milk crown, and it is found that the simulation reproduces the shapes changing drastically with the impact velocity.



Figure 5 Milk-crown formation

When dropping a droplet on a dry wall, the edge of the milk membrane jumps from the wall, which is typically observed in experiments (see Fig. 6).

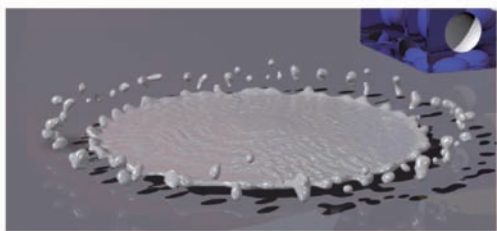


Figure 6 Dispersal of the milk on a dry wall.

Dam breaking into a wet floor

6

To check the simulation for more complex conditions, we studied the dam-break problem as a typical benchmark in collaboration with Prof. Hu's group of the Research Institute for Applied Mechanics, Kyushu University. By opening the shutter, the dam water launches onto a dry floor, and the speed of the water edge is often examined. In our experiment, the floor ahead of the dam was wet, and a violent wave breaking happened immediately since the inundating water was decelerated on the wet floor and the wave behind overtakes it.

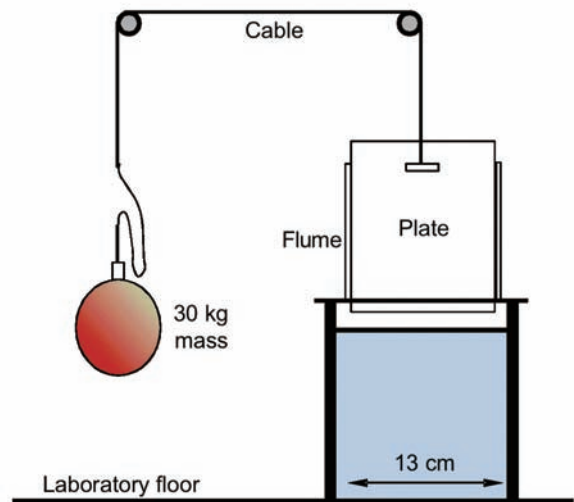
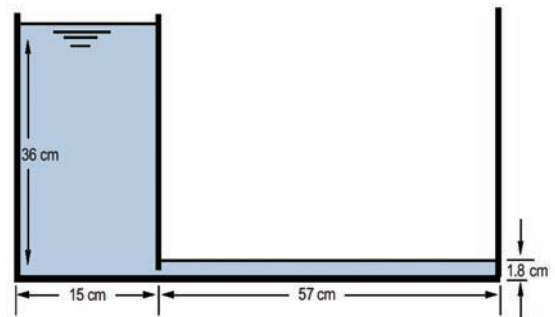


Figure 7 Setup of the dam-break experiment

In the vessel with the size of 72cm × 13cm × 36cm, water was filled to a height of 1.8 cm, and a dam that was 15 cm wide and 36 cm high was set initially. We show the time-evolving snapshots of the simulation results with 576 × 96 × 288 mesh in Fig.8. The last image is a snapshot of the experiment.

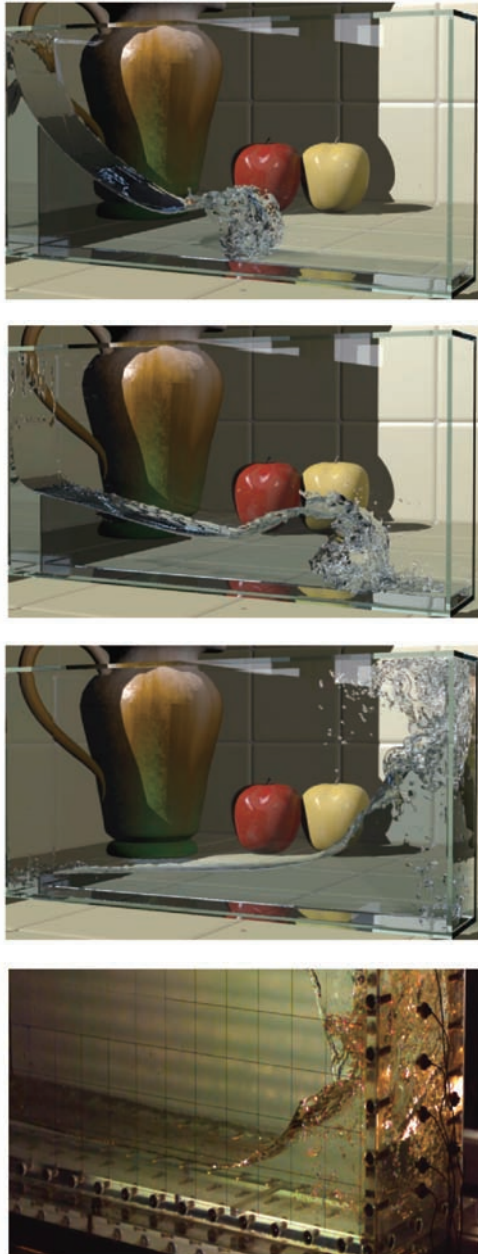


Figure 8 Simulation and experiment for dam-break problem

The simulation reproduces the wave breaking process well. When the water impacted with the side wall, it was found that many small bubbles are entrained into the water^[8]. This simulation is also available for evaluation of the damage caused by a tsunami impacting on a construction.

Multi-GPU computing

7

In our computation, all the components of the two-phase flow simulation have been implemented on CUDA code. The dependent variables such as flow velocity, pressure, Level-Set function, and VOF function were allocated on the on-board GPU memory. The GPU execution function calls were only requested from the host CPU, and we removed frequent CPU-GPU communication, which is a major overhead of GPU computing.

For a large-scale simulation, the computational domain is decomposed into small domains in which each GPU computation runs on the on-board video memory. Similar to multi-node CPU computing, it is required to communicate data among neighbor domains. The communication between the on-board memories of different GPUs consists of three steps through a host memory as shown in Fig. 9.

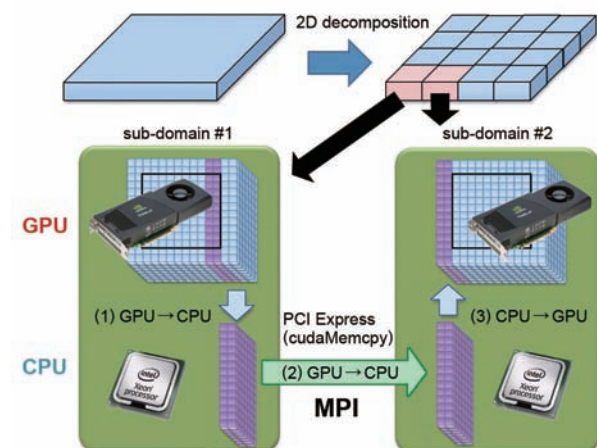


Figure 9 Data communication between domains for GPU computing.

Since the communication time between GPUs becomes a large overhead for large-scale GPU computing, we have introduced an overlapping technique between communication and computation^[9].

We used 60 nodes of TSUBAME 1.2 with two NVIDIA Tesla S1070s per node. The performances of the computations with mesh number 1923, 3843, and 7683 are plotted in Fig. 10. The 4 TFLOPS performance was achieved in single precision with 108 GPUs^[10].

A Large-scale Two-phase Flow Simulation on GPU Supercomputer

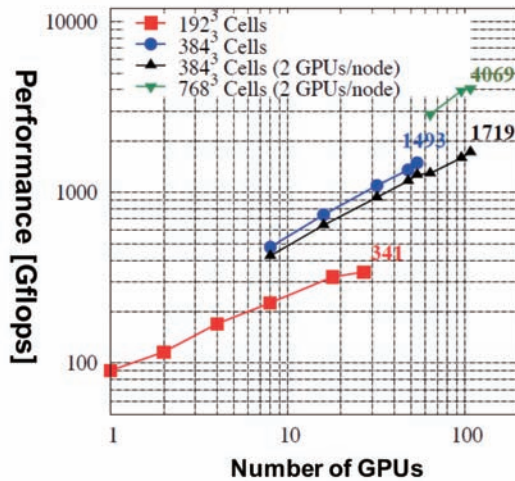


Figure 10 Performance of two-phase flow computations on multi-GPU computing.

Summary



Gas-liquid two-phase flow simulation is one of the challenging CFD topics, and we executed a simulation on the GPU supercomputer TSUBAME. A full GPU computation makes it possible to carry out large-scale computing that has never been done before. However, there are still problems to be solved, for example, sub-grid modeling of LES (large eddy simulation) for small bubbles in high-Reynolds turbulent flows.

Acknowledgements

This research was supported in part by KAKENHI, Grant-in-Aid for Scientific Research (B) 23360046 from The Ministry of Education, Culture, Sports, Science and Technology (MEXT), two CREST projects, "ULP-HPC: Ultra Low-Power, High Performance Computing via Modeling and Optimization of Next Generation HPC Technologies" and "Highly Productive, High Performance Application Frameworks for Post Petascale Computing" from Japan Science and Technology Agency (JST), and JSPS Global COE program "Computationism as a Foundation for the Sciences" from Japan Society for the Promotion of Science (JSPS).

References

- [1] M. Sussman, P. Smereka and S. Osher : A Level Set Approach for Computing Solutions to Incompressible Two-Phase Flow, *J. Comp. Phys.*, Vol. 114, pp.146-159 (1994)
- [2] C. W. Hirt, et al.: SOLA-VOF : A solution algorithm for transient fluid flow with multiple free boundaries , Los Alamos Scientific Laboratory, pp.1-32 (1980)
- [3] F. Xiao, Y. Honma and T. Kono : A simple algebraic interface capturing scheme using hyperbolic tangent function, *Int. J. Numer. Method. Fluid.*, Vol. 48, pp.1023-1040 (2005)
- [4] K.Yokoi : Efficient implementation of THINC scheme: A simple and practical smoothed VOF algorithm, *J. Comp. Phys.*, Vol. 226, pp.1985-2002 (2007)
- [5] J.R.Grace: *Transactions of the Institution of Chemical Engineers*, Vol. 51, pp.116-120 (1973)
- [6] M. van Sint Annaland, N.G.Deen and J.A.M.Kuipers: *Chemical Engineering Science*, Vol. 60, pp.2999-3011 (2005)
- [7] R. Krechetnikov and G.M. Homsy : Crown-forming instability phenomena in the drop splash problem, *J. Colloid Interface Sci.*, Vol. 331, pp.555-559 (2009)
- [8] Takayuki Aoki and Kenta Sugihara: Two-Phase Flow Simulation on GPU cluster using an MG Preconditioned Sparse Matrix Solver, *SIAM conference on Computational Science and Engineering 2011*, Reno, Nevada (2011)
- [9] T.Shimokawabe, T.Aoki, C.Muroi, J.Ishida, K.Kawano, T.Endo, A.Nukada, N.Maruyama, S.Matsuoka, "An80-fold-speedup,15.0 TFlops full GPU acceleration of non-hydrostatic weather model ASUCA production code" in *Proceedings of the 2010 ACM/IEEE International Conference for High Performance Computing, Networking, Storage and Analysis, SC'10*, IEEE Computer Society, New Orleans, LA, USA (2010)
- [10] Kenta Sugihara and Takayuki Aoki : Multi-GPU acceleration and strong scalability on a large-scale higher-order advection computation, the Japan Society for Computational Engineering and Science, *Transactions of JSCES*, Paper No.20100018 (2010)

Evolutionary Image/Video Coding with Massively Parallel Computing

Seishi Takamura

NTT Cyber Space Laboratories, NTT Corporation

Evolutionary methods based on genetic programming (GP) enable dynamic algorithm generation, and have been successfully applied to many areas such as plant control, robot control, and stock market prediction. On the other hand, conventional image/video coding methods such as JPEG, MPEG-2, MPEG-4 and AVC/H.264 all use fixed (non-dynamic) algorithms without exception. To relax this limitation, GP has been successfully applied to dynamic generation of pixel prediction algorithm. However, one of the challenges of this approach is its high computational complexity. In this article, we introduce a GP-based image predictor that is specifically evolved for each input image, its good match with parallel computing, and some of speeding-up approaches, which includes the use of massively parallel computation such as TSUBAME2.0 and GPGPU.

Introduction and Motivation

1

In image/video coding schemes such as JPEG and AVC/H.264, the prediction mode, quantization parameter, prediction coefficients, context grouping thresholds, etc. are adaptively chosen to optimize the compression performance. So are motion vectors and prediction modes in video coding. In current image/video coding schemes, these “coding parameters” are dynamically optimized. However, the “coding algorithm” itself is never altered within the scheme. In other words, there has been no way to develop a new coding scheme other than by human implementation via the trial and error approach. Therefore, codec complexity cannot exceed what humans are capable of. Furthermore, it has not been realistic to develop content-specific (not even image-category-specific) coding algorithms. Our target then is to develop a scheme that allows a computer to generate content-specific image/video coding algorithms. In this overview, we introduce several latest activities on this evolutionary approach.

Evolution Process Description and Performance

2

The Genetic Algorithm (GA) is one approach to optimization problems; it arranges the “solution parameter” as a one-dimensional array (a gene). It iterates the emergence of generations via survival of the fittest to obtain a practical solution parameter. Genetic Programming (GP)^[1], on the other hand, creates a gene tree-structured to enable “solution method” optimization. Such methods, which are inspired by organic evolution, are called “evolutionary methods”, and have been applied to a wide range of fields such as plant control, stock market prediction, robot control, and analog circuit design.

As for codec applications of the evolutionary method, Tanaka et al. evolved a “context template” for binary image coding^[2]. Takagi et al. evolved “region segmentation” for video coding^[3]. They both use GA for parameter (context template or region segmentation) optimization, while their coding algorithms remain fixed.

2-1 Methodology

GP-based methods enable dynamic algorithm generation, and have been successfully applied to many areas such as plant control, robot control, and stock market prediction. We introduce a GP-based image/video coding approach that is specifically evolved for each input image. Following is the method of automatic nonlinear image predictor generation^[4,5].

We express the prediction algorithm using the tree expression. The tree is consisted of leaf nodes (such as immediate values, surrounding pixel values and the coordinates of the pixel to be predicted) and non-leaf nodes (such as math functions (e.g., add, cos), operations (e.g., min, max) and conditional branches). Then, we initialize the population with randomly generated individuals (i.e., trees or prediction algorithms) and common predictors such as MED^[6] or GAP^[7]. The predictor is evolved through the well-known GP procedure (i.e., parent selection, children generation (crossover and mutation) and survival selection). We use the minimal generation gap method^[8] for creating the generations.

For the quantitative metric that measures “how good the individual (i.e., the predictor) is”, we use the sum of two information amounts, $IT + IR$ [bits]. IT is the amount of tree information that represents the predictor's algorithm; it equals the sum of the information of each node in the tree. IR is the amount of residual (prediction error) signals' information.

2-2 Prediction Performance

We used four 512x512, 8-bit, gray-scale images (Lena, Baboon, Airplane, Peppers) for experiment. We tested two evolutionary predictors, EP4 and EP12. EP4 uses four adjacent pixels. EP12 uses

12 adjacent pixels. For all predictors, the prediction residual was applied CALIC's edge-based context separation method^[7] to reduce the entropy. The results are shown in Table 1. In the table, LS(n) means least-square predictor using surrounding n pixels, LE(n) means the least-entropy predictor using surrounding n pixels (the prediction coefficients are optimized off-line to yield the lowest entropy). It is observed that evolutionary predictor offers better prediction performance than other methods. Especially, EP4 is even better than LE(12).

Average predictor size for EP12 was 2062.2 [bits]. As an example, Peppers' predictor is shown in Fig. 1. The predictor includes many mathematical expressions which are beyond human's imagination.

Predictor	Lena	Baboon	Airplane	Peppers	Avg.(incr.)
LS(4)	4.551	5.521	3.654	4.465	4.548(5.6%)
LS(12)	4.549	5.374	3.635	4.410	4.492(4.3%)
LE(4)	4.529	5.506	3.619	4.417	4.517(4.9%)
LE(12)	4.522	5.361	3.595	4.382	4.465(3.6%)
GAP(4)	4.539	5.556	3.568	4.468	4.533(5.2%)
MED(3)	4.692	5.592	3.644	4.646	4.643(7.9%)
EP4	4.481	5.462	3.521	4.352	4.454(3.4%)
EP12	4.385	5.175	3.411	4.262	4.308

Table 1. Residual entropy (overhead inclusive) of the predictors, their increment ("incr." in percentage) against EP12. Numbers next to the predictors mean the number of reference pixels

2-3 Criteria Tweak

In above, we used the criteria which is the sum of tree size and residual size (i.e., IT + IR). By tweaking the criteria to be minimized, new features are embodied.

(a) Generation of fast codec

We incorporated encoding time(EncTime) and decoding time (DecTime) of the individual to the criteria

$$IT + IR + \lambda_1 EncTime + \lambda_2 DecTime$$

By tweaking λ_1 and λ_2 , we successfully generated fast encoder or fast decoder while balancing its coding performance^[9].

(b) Tree-size penalty

Since IT is taken into account in the criteria to be minimized, excessive growth of the tree (so called bloat) is somewhat suppressed. However, sometimes larger trees have chance to survive. Suppose there are two predictors (larger and smaller) of the same coding performance. It is less efficient to enhance larger tree than to enhance smaller tree, because of the bigger search space of the larger tree.

Instead of using IT + IR criteria, we applied the weight (w) to IT [10]. i.e., the new criteria is set to be

$$w IT + IR$$

The result is shown in Fig. 2. It is clearly seen that applying penalty yields faster evolution and more compact tree.

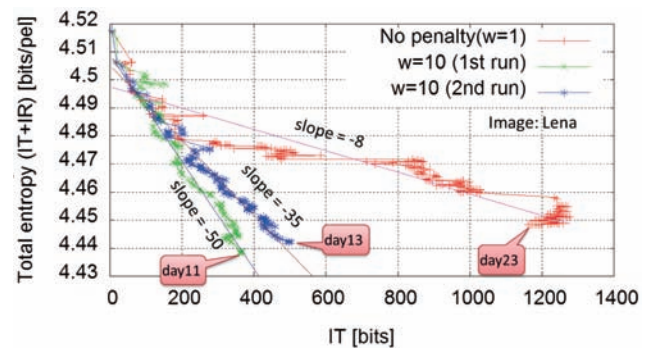


Figure 2 The growth of the tree (from top to downward) with/without tree-size penalty.

```

Peppers: if  $D - I_{10} \geq 0$  then  $I_{gap} \leftarrow \text{Pred0}$ 
else if  $-D - 31.1797 \geq 0$  then  $0.50196[\text{xor}(\min(\max(I_{03}, 0.578125(D + I_{00} + I_{02})), |I_{07} - I - \max(I_{00}, \text{if } x \geq 0 \text{ then } \rho \text{ else } \min(90.7501, I_{01})) + 2.5939|), I_{01})] + 0.50196 I_{gap} \leftarrow \text{Pred1}$ 
else if  $-\sqrt{|I_{11} - I_{02}|} - \sqrt{|I_{10} - I|} + \min(|D| - I_s/2 - 75.91195|, I_{07}, I_{09}/2 + I_{00}/2) + \theta - \max(I_{03}, I_{00}, I_{07}) + 29.498 \geq 0$  then  $0.75147 [0.28107 [0.54697 [0.24244 I_{09} - 0.70967 [|I_{04} - I_{00} - I_s| - I_{02} + I_s|] + 0.18145 [|I_{07} - I_{04} + I_{00}| - I_{05} + I_{03}| - 0.23255 I_{04} + 1.59610 | + 0.09227 I_{06} - 0.617188 I_{00} - 0.24171 I_{03}] + 0.21722 I_{03} + 0.25049 I_{01}] \leftarrow \text{Pred2}$ 
else or  $(\min(I_{gap}, \max(\min(I_{02}, |I + y + \min(I_{01}, I_{03}, |I + I_s| - I_{06}) - I_{08}, I_{10}^2), I_{09})), |I_{07} - |\tan x| - I_{00} - I_{02} - I_s|/2) / 2 + I_{gap}/2) \leftarrow \text{Pred3}$ 

```

Figure 1. Generated predictor (EP12) for Peppers and its conditional branch structure. I_{xx} are surrounding pixel values. See^[5] for more detail of the variables

Evolution Acceleration

3

Though recent computing processors offer greater and greater processing capability, the algorithm generation still requires considerable amount of time. As the predictor grows in size and complexity, the execution time of the fitness function for a single predictor increases by several orders of magnitude. Therefore, acceleration of the evolution computation is strongly demanded. Evolutionary algorithm generation fits quite well with parallel processing. One example of parallel evolution using multiple processors/cores is shown in Fig. 3. Each processor/core does evolution independently, while occasionally observing the globally-best individual kept in a shared file. Unlike some parallel processing applications, there is no need to synchronize each process. Therefore each core works in 100 % load, and addition/subtraction of processors/cores is quite easy. In addition, there is also no need to have processors/cores homogeneous.

3-1 Acceleration with TSUBAME, a parallel computing cluster

The supercomputer TSUBAME of Tokyo Institute of Technology^[11] kindly offered us trial use of it. It has AMD Dual-Core Opteron 2.4GHz, 8CPU, 32GB memory, operating system of SUSE Linux Enterprise Server 10 (x86_64) Patchlevel 2. Among its more than 10,000 cores, we are allocated about 1,500 cores for the experiment. In 2010, it has been upgraded to TSUBAME2.0, whose thin nodes have Intel Xeon X5670 2.93GHz, 12cores/24threads for each, operating system of SUSE Linux Enterprise Server 11 (x86_64) SP1.

Among its more than 15,000 cores, we used 2,400 cores for the experiment.

Figs. 4 and 5 show the experimental results. The evolution acceleration due to the number of the cores is apparent. To evaluate the effectiveness of parallel processing, the time to reach certain bit rate (4.407 bits/pel) is shown in Table 2. Its right column shows the speed-up factor vs. single-core processing. The relation between number of cores and speed-up factor is depicted in Fig. 6. Almost linear relation is clearly observed.

3-2 Acceleration with GPU

Advances in GPU hardware in the last several years have significantly improved their effectiveness for highly parallelizable programs. Because the fitness function evaluates the predictor for each pixel in the image, it is an ideal application for the GPU architecture.

We implemented evolutionary process into GPU using CUDA platform^[12]. We conducted the experiment on a single server with dual Xeon X5670 2.93 GHz processors (six cores each), four NVIDIA Tesla C2050 graphics cards (448 CUDA cores each), and 24 GB of memory. Operating System is Ubuntu Server Edition 10.04 (64-bit), and C/C++ compiler is GCC 4.4. For timing individual predictors, a single CPU core was timed against one Tesla C2050 paired with one CPU core. For predictor evolution, four CPU cores were timed against four Tesla C2050s, each paired with one CPU core. The result is shown in Table 3. Throughout various predictor sizes, GPU achieved ~140x speed-up consistently.

For image Lena, times to reach 4.493 [bits/pel] were 18.86 hours for CPU and 217 seconds for GPU. In this case GPU achieved 312x times faster evolution. Its performance transition is shown in Fig.7.

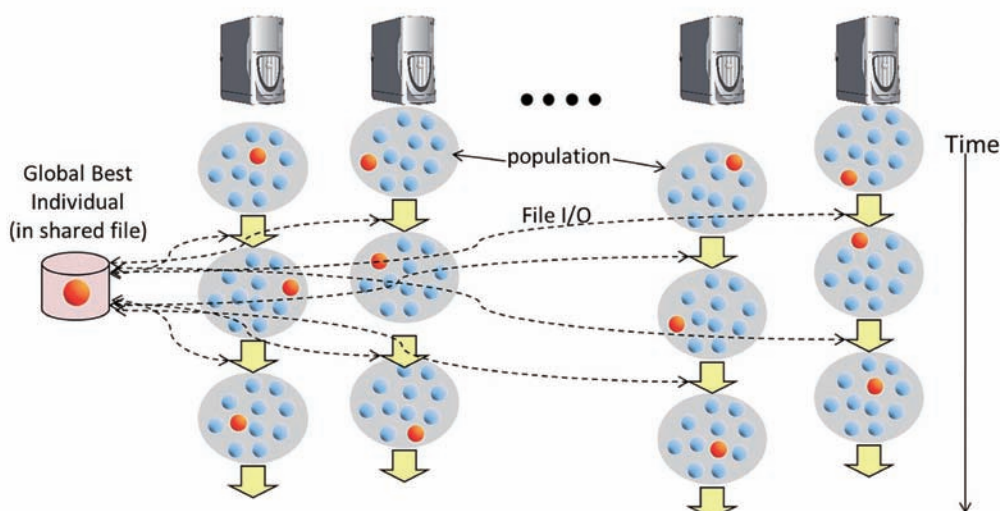


Figure 3 An image of parallel evolution

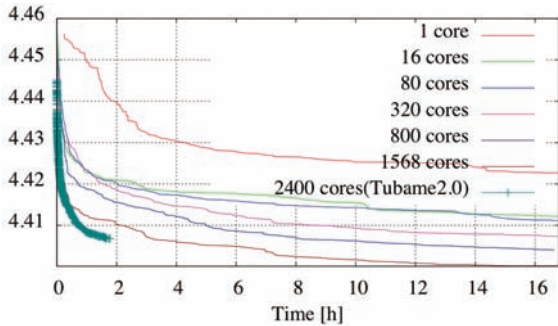


Figure 4 Compression performance transition with different parallelization degrees

#cores	Time (hours)	Speed-up factor (vs. one thread)
1	2075.3	1
16	129.7	16.0
80	67.78	30.6
320	19.02	109.1
800	7.98	260.1
1,568	3.10	669.4
2,400	1.80	1152.9

Table 2 Time taken to reach 4.407 bits/pel and speed-up factor

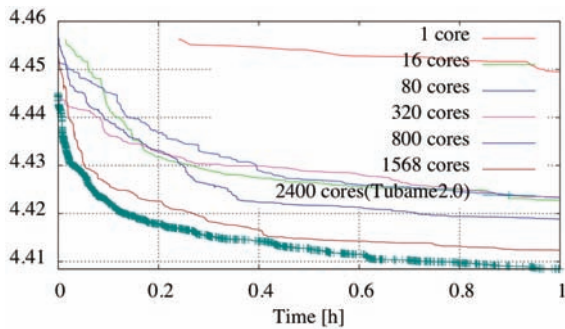


Figure 5 Partially magnified version of Fig. ST4 (up to 1 hour)

predictor size [nodes] / info. (IT) [bits]	CPU [msec]	GPU [msec]	speed-up factor (vs. CPU)
240 / 1631	1195	8.0277	148.8x
345 / 2251	1882	13.429	140.2x
422 / 2719	2311	16.564	139.5x
469 / 3079	2692	18.724	143.8x

Table 3 Timings and speed-up factors for Lena

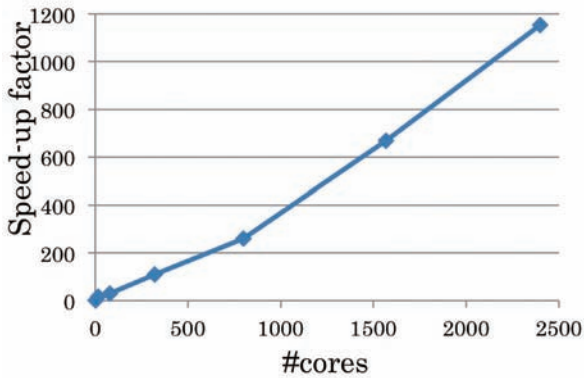


Figure 6 Speed-up factor according to the number of cores

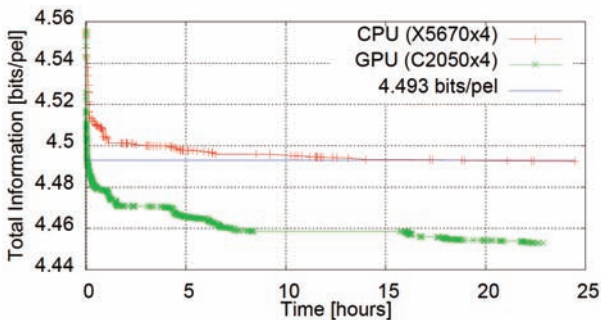


Figure 7 Evolutionary predictor's performance transition for Lena. Red: CPU, green: GPU

3-3 Acceleration with class separation

We have seen that the evolved predictor sometimes consists of conditional branches. For example, the evolved predictor for image Peppers had the following structure (see Fig. 1):

```

for each pixel
if (Condition0) Pred0
else if (Condition1) Pred1
else if (Condition2) Pred2
else Pred3
    
```

According to these conditions, the predictors (Pred0...3) are switched pixel-by-pixel. A distribution map of those predictors is shown in Fig. 8. Apparently, horizontal edges, vertical edges, highlight areas and the rest are predicted by distinct predictors. It can be considered that the predictor is evolved so that it adapts to local image properties (e.g., edge direction and flatness), which turns out to enhance the prediction performance.

Inspired by the behavior of the evolutionary predictor, we actively classify each pixel according to its local edge direction. We classified into nine classes: eight classes for eight edge directions and one class for flat area (see Figs. 9 and 10 as the example for the image Peppers). For each class, we evolve the predictor independently^[13]. The time taken to reach these bit rates is shown in Table 4. It is observed that the speed-up factor for the proposed method against the conventional method was quite drastic; 25.4-344.0 (average 180.1x). See Fig. 11 for detailed transition for Peppers.

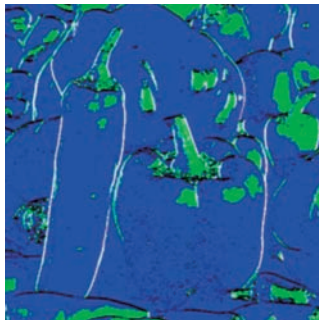


Figure 8 Predictor distribution map for Peppers. Each color (white, blue, green and black) corresponds to a distinct predictor

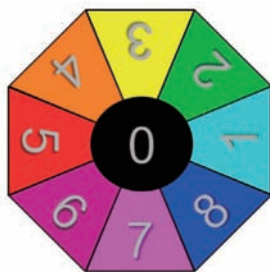


Figure 9 Local edge direction and associated class

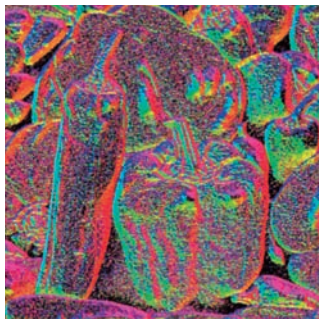


Figure 10 classification map (the color corresponds to Fig. 9) for Peppers.

Image	Target bit rate [bits/pel]	Processing time [mins]		Speed-up factor	Predictor size (IT) [bits]	
		Conventional	Proposed		Conventional	Proposed
Lena	4.435	3638.5	21.3	170.8x	691.6	807.9
Peppers	4.263	4093.9	11.9	344.0x	1628.7	1094.7
Baboon	5.200	953.6	37.5	25.4x	549.4	1452.6
Avg.				180.1x	956.6	1118.4

Table 4. Time taken (in minutes) to reach certain bit rate, speed-up factor and predictor size

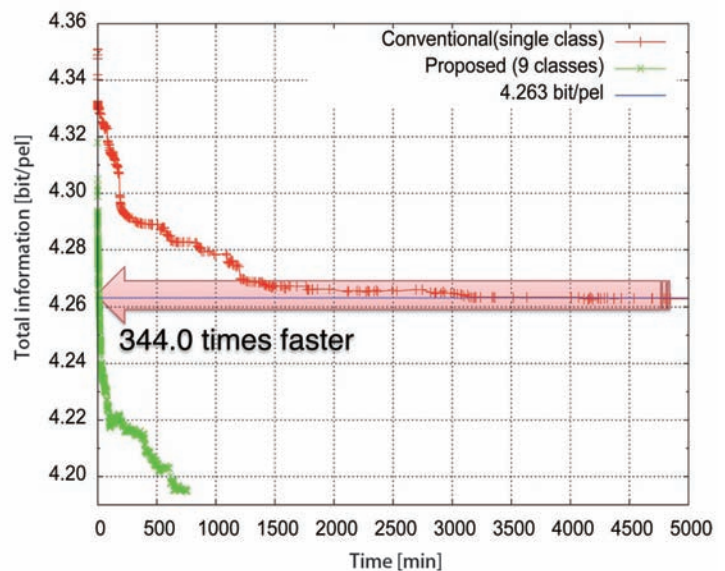


Figure 11 Evolutive predictor's performance transition. Red: conventional, green: proposed (image = Peppers)

Discussion and Future Vista

4

4-1 On ultimate compression

Quite interestingly, Fig. 2 reveals a linear relationship between the tree size and coding performance. We have observed that every trial had the same tendency. Therefore it is conjectured that

$$IT + IR = \text{rate} + k IT$$

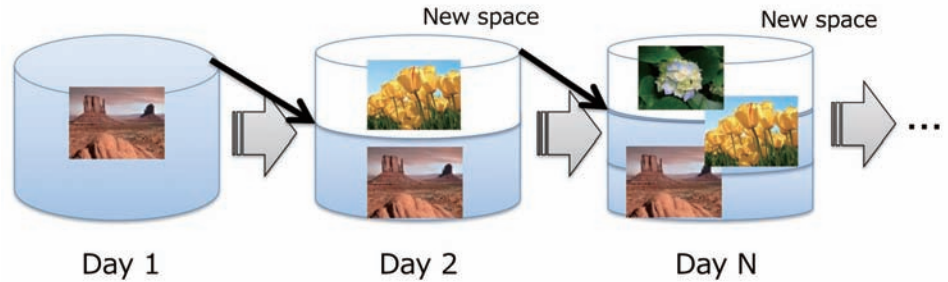
where $k = -50 \dots -35$ (the slope in Fig. 2). For typical lossless compression, $\text{rate} = \sim 4$ [bits/pel] (about half of original size).

Since $IT \geq 0$ and $IR \geq 0$, ultimate compression rate is attained when $IR = 0$ (no residue; i.e., the predictor itself contains image information). Then we have ultimate rate as

$$IT + IR (= IT) = \text{rate} / (1 - k).$$

This rate (about 1 % of original size) sounds too low for lossless coding. It should be noted that the coding rate is bounded by the amount of the noise in an image, since the noise is incompressible by nature. However, it is still conjectured that the ultimate compression rate is close to the noise amount (then the prediction residual becomes the white noise completely). Another thing which should be noted is, the evolution speed exponentially slows down according to the value of IT. So currently it is not expectable to reach such an ultimate point.

Figure 13 An image of self-compressing archive



4-2 Reverse-engineering of Image

Further extrapolation of above discussion bethinks us that ultimate predictor is an indication of the model that is hidden behind the image data. Following is the minimum toy experiment to see if GP is powerful enough to reveal such an image model. Three images were generated from simple model (see Fig.12).

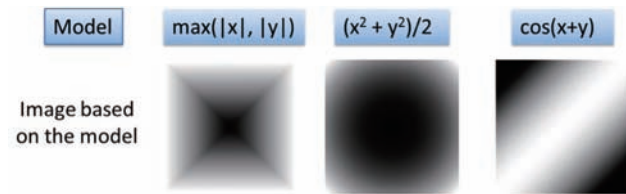


Figure 12 Simple models and associated images

Then, only the image (not the model) was fed into the evolutive predictor generator. The outcomes were:

$$\max(|y|, |x|), |(x^2+y^2)/2|, \cos(x+y)$$

respectively. They are all mathematically equivalent to the given model. In other words, reverse-engineering of the image would be attained using evolutive coding.

4-3 Self-compressing archive

One of the applications of evolutive coding is its combination with image/video archive. Making use of excessive computational power from e.g., the cloud, the archive updates its coding algorithm day by day, and the size continuously shrinks to yield a space to archive other images (Fig. 13).

4-4 Category-specific coder

Until here, image-specific algorithm generation has been discussed. It would be nice if a certain algorithm performs reasonably well for an image of certain pre-defined category.

We prepared three categories (clouds, city lights and nature)^[14]. Each category contains ten 128 x 128 gray scale images. The anchor scheme was generated which offers the lowest average coding rate for all 30 images. Similarly, the evolutionary process was conducted for each category, and for each image respectively.

category	anchor	for category	for image	JPEG2000
clouds	2.925	2.884(-1.4%)	2.887(-1.3%)	3.142(6.9%)
city lights	5.507	5.496(-0.2%)	5.499(-0.2%)	6.029(8.7%)
nature	6.406	6.387(-0.3%)	6.389(-0.3%)	6.846(6.4%)

Table 5. Bit rates and increase against the anchor (in parentheses)

Table 5 shows the simulation results. Image-specific coder ("for image") is the best as expected. However, category-specific coder ("for category") offers only slight performance loss (~0.1%).

4-5 Application to lossy coding

Evolutive image/video coding can be applied not only to lossless coding but also to lossy coding. By generating content-specific nonlinear image restoration filter using GP, about 0.9% coding rate reduction against HEVC, state-of-the-art coding technology under development, is achieved^[15].

Summary

5

In this article, evolutive image/video coding was introduced regarding its concept, characteristics, potential and future vista. In particular, its fitness to the parallel processing system such as TSUBAME/TSUBAME2.0 would surely extend its feasibility. Therefore the advance of such a high-performance computing platform is tightly connected to the advance of evolutive image/video coding.

References

- [1] J. Koza, "Genetic Programming II, Automatic Discovery of Reusable Programs," The MIT Press, (1998)
- [2] M. Tanaka, H. Sakanashi, M. Mizoguchi, T. Higuchi, "Bi-level image coding for digital printing using genetic algorithm," Electronics and Communications in Japan part III: Fundamental Electronic Science, vol. 84, no. 9, pp. 1-10, (Apr. 2001)
- [3] K. Takagi, A. Koike, S. Matsumoto and H. Yamamoto, "Motion Picture Coding Based on Region Segmentation Using Genetic Algorithm," Systems and Computers in Japan, vol. 33, no. 5, pp. 41-50, (Mar. 2002)
- [4] S. Takamura, M. Matsumura and Y. Yashima, "Automatic Pixel Predictor Construction Using an Evolutionary Method," Proc. PCS2009, pp. 1-4, (May 2009)
- [5] S. Takamura, M. Matsumura and Y. Yashima, "A Study on an Evolutionary Pixel Predictor and Its Properties," Proc. ICIP2009, (Nov. 2009)
- [6] "Lossless and Near-Lossless Compression of Continuous Tone Still Images," ISO/IEC 14495-1, (2000)
- [7] X. Wu and N. Memon, "Context-Based, Adaptive, Lossless Image Coding," IEEE Trans. Commun. vol. 45, no. 4, pp. 437-444, (Apr. 1997)
- [8] H. Satoh, M. Yamamura and S. Kobayashi, "Minimal Generation Gap Model for GAs Considering both Exploration and Exploitation," Proc. 4th Int. Conf. Soft Computing, pp. 494-497, (Oct. 1996)
- [9] M. Matsumura, S. Takamura and H. Jozawa, "Evolutive Image Coding Based on Automatic Optimization for Coding Tools Combination," Proc. IWAIT2010, (Jan. 2010)
- [10] S. Takamura, "Evolutive Video Coding ~From Generic Algorithm towards Content-Specific Algorithm~, " PCS2010 tutorial talk (T1), (Dec. 2010)
- [11] <http://www.gsic.titech.ac.jp/en>
- [12] M. McCawley, S. Takamura and H. Jozawa, "GPU-Assisted Evolutive Image Predictor Generation," IEICE Tech. Rep., vol. 110, no. 275, IE2010-88, pp. 25-28, (Nov. 2010)
- [13] S. Takamura, M. Matsumura and H. Jozawa, "Accelerating Pixel Predictor Evolution Using Edge-Based Class Separation," Proc. PCS2010, P1-22, pp. 106-109, (Dec. 2010)
- [14] M. Matsumura, S. Takamura and H. Jozawa, "Generating Subject Oriented Codec by Evolutionary Approach," Proc. PCS2010, P3-13, pp. 374-377, (Dec. 2010)
- [15] S. Takamura and H. Jozawa, "A Basic Study on Automatic Construction of Nonlinear Image Denoising Filter", Proc. PCSJ2011, (Oct. 2011) [to appear]

● TSUBAME e-Science Journal No.4

Published 10/31/2011 by GSIC, Tokyo Institute of Technology ©
ISSN 2185-6028
Design & Layout: Kick and Punch
Editor: TSUBAME e-Science Journal - Editorial room
Takayuki AOKI, Thirapong PIPATPONGSA,
Toshio WATANABE, Atsushi SASAKI, Eri Nakagawa
Address: 2-12-1-E2-1 O-okayama, Meguro-ku, Tokyo 152-8550
Tel: +81-3-5734-2087 Fax: +81-3-5734-3198
E-mail: tsubame_j@sim.gsic.titech.ac.jp
URL: <http://www.gsic.titech.ac.jp/>

TSUBAME

International Research Collaboration

The high performance of supercomputer TSUBAME has been extended to the international arena. We promote international research collaborations using TSUBAME between researchers of Tokyo Institute of Technology and overseas research institutions as well as research groups worldwide.

Recent research collaborations using TSUBAME

1. Simulation of Tsunamis Generated by Earthquakes using Parallel Computing Technique
2. Numerical Simulation of Energy Conversion with MHD Plasma-fluid Flow
3. GPU computing for Computational Fluid Dynamics
4. Numerical Parameterization of Aerodynamic Properties in Urban Area
Based on a Very Large Scale Simulation of Urban Flow Field
5. Large-scale Hemodynamics Computation on GPU

Application Guidance

Candidates to initiate research collaborations are expected to conclude MOU (Memorandum of Understanding) with the partner organizations/ departments. Committee reviews the "Agreement for Collaboration" for joint research to ensure that the proposed research meet academic qualifications and contributions to international society. Overseas users must observe rules and regulations on using TSUBAME. User fees are paid by Tokyo Tech's researcher as part of research collaboration. The results of joint research are expected to be released for academic publication.

Inquiry

Please see the following website for more details.
<http://www.gsic.titech.ac.jp/en/InternationalCollaboration>

